nature COMMUNICATIONS

ARTICLE

Received 31 Aug 2016 | Accepted 28 Feb 2017 | Published 5 May 2017

DOI: 10.1038/ncomms15167 OPEN

Wide bandgap $BaSnO_3$ films with room temperature conductivity exceeding 10^4 S cm^{-1}

Abhinav Prakash[1], Peng Xu[1], Alireza Faghaninia[2], Sudhanshu Shukla[3,4], Joel W. Ager III[3,5], Cynthia S. Lo[2] & Bharat Jalan[1]

Wide bandgap perovskite oxides with high room temperature conductivities and structural compatibility with a diverse family of organic/inorganic perovskite materials are of significant interest as transparent conductors and as active components in power electronics. Such materials must also possess high room temperature mobility to minimize power consumption and to enable high-frequency applications. Here, we report n-type $BaSnO_3$ films grown using hybrid molecular beam epitaxy with room temperature conductivity exceeding 10^4 S cm^{-1}. Significantly, these films show room temperature mobilities up to 120 cm^2 V^{-1} s^{-1} even at carrier concentrations above 3×10^{20} cm^{-3} together with a wide bandgap (3 eV). We examine the mobility-limiting scattering mechanisms by calculating temperature-dependent mobility, and Seebeck coefficient using the Boltzmann transport framework and *ab-initio* calculations. These results place perovskite oxide semiconductors for the first time on par with the highly successful III–N system, thereby bringing all-transparent, high-power oxide electronics operating at room temperature a step closer to reality.

[1] Chemical Engineering and Materials Science, University of Minnesota–Twin Cities, Minneapolis, Minnesota 55455, USA. [2] Department of Energy, Environmental, and Chemical Engineering, Washington University, St Louis, Missouri 63130, USA. [3] Materials Sciences Division, Lawrence Berkeley National Laboratory, Berkeley, California 94720, USA. [4] Energy Research Institute, Interdisciplinary Graduate School, School of Materials Science and Engineering, Nanyang Technological University, 50 Nanyang Avenue, Singapore 639798, Singapore. [5] Materials Science and Engineering, University of California at Berkeley, Berkeley, California 94720, USA. Correspondence and requests for materials should be addressed to A.P. (email: praka019@umn.edu) or to B.J. (email: bjalan@umn.edu).

Wide bandgap ternary oxides with perovskite structure have generated considerable excitement due to their impressive multi-functionality and the promising route they provide to potentially disruptive technologies for logic and resistive memory, utilizing both electronic and spintronic concepts[1–4]. Rapid progress with perovskite oxide heterostructures has also been made, including demonstration of strain-stabilized non-equilibrium electronic and magnetic properties, two-dimensional electron gas formation, quantum oscillation effects, and exotic magnetism and superconductivity[5]. However, the realization of this staggering range of functionalities at room temperature remains a grand challenge in the field. Carrier mobility in semiconducting perovskite oxides provides an ideal, and very technologically important, example[6].

The best room temperature values of the mobility and conductivity in the model perovskite oxide semiconductor $SrTiO_3$ have remained below $10\,cm^2\,V^{-1}\,s^{-1}$ and $500\,S\,cm^{-1}$, respectively for over 50 years[6]. Well-publicized advances with interfaces such as $LaAlO_3/SrTiO_3$ have similarly been restricted to low temperatures[5]. Very recently, bulk $BaSnO_3$ (BSO) has shown significantly higher room temperature mobilities and corresponding conductivities. Luo *et al.*[7], first discovered a room temperature mobility of $103\,cm^2\,V^{-1}\,s^{-1}$ at a carrier concentration of $8\times10^{19}\,cm^{-3}$ in bulk doped BSO crystals followed by the work of Kim *et al.*[8,9] showing a much higher mobility of $320\,cm^2\,V^{-1}\,s^{-1}$ and a conductivity value of $4\times10^3\,S\,cm^{-1}$ at a carrier concentration of $8\times10^{19}\,cm^{-3}$ (refs 8,9). Owing to these behaviours, doped BSO has gained significant interest as a high-performance transparent conductor[7–12]. A favourable conduction band offset of BSO with structurally similar oxides such as $SrTiO_3$ (STO) and $LaAlO_3$ (LAO) further makes it a promising candidate for high mobility channel material in oxide heterostructures for both power electronic applications and fundamental physics study[6,13–15].

However, thin films of BSO have shown significantly lower mobilities. The highest reported mobility in thin films grown using molecular beam epitaxy (MBE) is $150\,cm^2\,V^{-1}\,s^{-1}$ on $PrScO_3$ (110) at a carrier concentration of $7.2\times10^{19}\,cm^{-3}$, decreasing to $80–120\,cm^2\,V^{-1}\,s^{-1}$ for films on STO (001) between $6\times10^{19}–1\times10^{20}\,cm^{-3}$, which results in an overall conductivity of $2\times10^3–3\times10^3\,S\,cm^{-1}$ (ref. 16). The difference in mobility between bulk single crystals and thin films of BSO has been largely attributed to the substrate-induced misfit/threading dislocations[16]. Dislocations can introduce charged defects leading to compensation of carriers, and an overall reduced mobility. For instance, threading dislocation cores in GaN have been shown to consist of Ga-vacancy (V_{Ga}) based defect complexes[17], which form deep compensating acceptors[18,19] together with space charge regions around the dislocation lines, resulting in enhanced electron scattering and thus reduced mobility[20].

A similar effect can be expected from non-stoichiometry[21], which also introduces charged point defects. Evidence that this effect is often at play in BSO is the observation of different mobility values for films grown via different synthesis routes despite having similar substrates and doping levels[7,9,22,23]. Even homoepitaxial films[24] show much lower mobility compared to bulk single crystals suggesting an important role of point defects. Furthermore, films grown by MBE show a large variation in the mobility values despite having identical carrier concentration[16]. These results raise the question of how non-stoichiometry and dislocations in films influence electronic transport. It further begs the question as to what scattering mechanisms limit the electron mobility and therefore the conductivity in BSO films and what can be the ultimate mobility in BSO if defects are minimized. It is also noteworthy that there are no transport studies in BSO below a doping level of $10^{19}\,cm^{-3}$ raising further questions regarding the identity of the compensating defects.

To understand the role of dislocations, non-stoichiometry, and chemical dopants on electronic transport, and to examine mobility-limiting scattering mechanisms in doped BSO, we combine experiments and modelling using the Boltzmann transport and density functional theory (DFT) calculations. First, we investigate the influence of dislocations on the carrier concentration and mobility in doped BSO by tailoring the dislocation density by varying undoped buffer layer thickness. Second, we investigate the role of charge compensation on the critical density for the metal-to-insulator transition, carrier concentration, mobility and the Seebeck coefficient. Finally, we calculate the band structure, mobility and Seebeck coefficient to shed light on the scattering mechanisms limiting the mobility at different carrier concentrations and temperatures and provide the upper limits for mobility in a dislocation-free material.

Results

Thickness optimization of buffer and active layers. All BSO/STO heterostructures were prepared using hybrid MBE. Growth conditions were chosen to yield phase pure, epitaxial and stoichiometric films on STO substrates[21,25]. (See Supplementary Figs 1 and 2 for X-ray diffraction pattern and atomic force micrograph). The lattice mismatch of BSO is -5.12% (compressive) with the STO(001) substrate, resulting in the formation of misfit dislocations and strain relaxation for films with thickness above 1 nm (ref. 25). The density of misfit dislocations is largest near the film/substrate interface, which reduces the carrier mobility and also affects defect densities. Inserting a thick insulating (undoped) buffer layer between the substrate and the doped (active) layer may reduce the defect density in doped layers grown on top of it[26]. It must, however, be noted that dislocations remain present in doped layers as threading dislocations[25], which are inevitable without a lattice-matched substrate.

To investigate the role of dislocations on the electronic transport, we grew a series of 31 nm La-doped BSO/t_{buffer} BSO/STO(001) films, as illustrated in the inset of Fig. 1a. Here, we fix the thickness of the active layer for which the transport will be evaluated while varying t_{buffer} between 30 and 250 nm. Dopant density in the active layer was kept constant by fixing the La-cell temperature (T_{La}) at 1230 °C. Figure 1a shows room temperature carrier concentration (n_{3D}) and mobility ($\mu_{300\,K}$) as a function of t_{buffer}. n_{3D} increases monotonically between $2.5\times10^{20}\,cm^{-3}$ and $4\times10^{20}\,cm^{-3}$ whereas $\mu_{300\,K}$ first increases to $115\,cm^2\,V^{-1}\,s^{-1}$ at $t_{buffer}=124$ nm and then decreases. The fact that n_{3D} increases with increasing t_{buffer}, which in turn decreases dislocation density in active layer (See Supplementary Fig. 3) suggests charge compensation being operative, and that threading dislocations act as acceptor-like defects. We interpret the decrease in $\mu_{300\,K}$ for $t_{buffer}>124$ nm is due to scattering from increased surface roughness (See Supplementary Fig. 4)[27]. Having determined the optimal buffer layer thickness which is similar to what has been reported by Park *et al.*[27], we then grew a series of t_{active} La-doped BSO/124 nm BSO/STO(001) films keeping the dopant density ($T_{La}=1230$ °C) fixed (Fig. 1b). No significant change in n_{3D} and $\mu_{300\,K}$ was observed indicating no surface depletion effect or enhanced scattering at the buffer/active interface. That is, the active layer appears to be spatially uniform from a transport point of view. For rest of the study, we have chosen $t_{buffer}=124$ nm and $t_{active}=124$ nm unless otherwise stated.

Metal-insulator transition and charge compensation in doped BaSnO3 films. To systematically investigate the effect of charge compensation due to dislocations on electronic transport, we

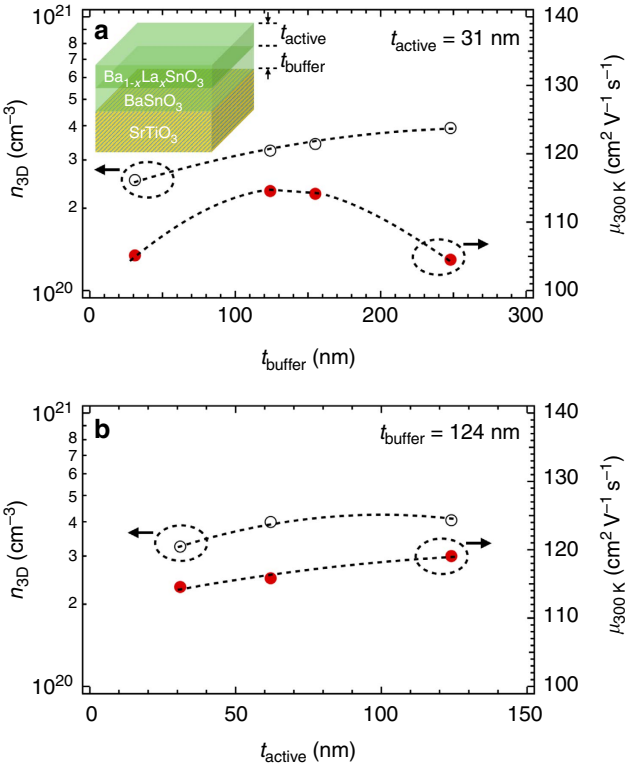

Figure 1 | Effect of buffer and active layer thicknesses on room temperature carrier density and mobility. Variation of n_{3D} (black open circles) and $\mu_{300\,K}$ (red solid circles) in doped $BaSnO_3$ films as a function of (**a**) t_{buffer} for fixed $t_{active}=31$ nm, and (**b**) t_{active} for fixed $t_{buffer}=124$ nm. Inset shows a schematic of the structure.

prepared a doping series of 124 nm $Ba_{1-x}La_xSnO_3$/124 nm BSO/STO(001) heterostructures. The value of x, and thereby n_{3D} was controlled by varying T_{La} at a fixed Ba/Sn beam equivalent pressure (BEP) ratio. The oxygen flux was also kept fixed. Figure 2a shows the resistivity (ρ) versus T as a function of n_{3D}. Dashed line in Fig. 2a at 0.06 Ω-cm corresponds to the calculated values of ρ for metal-to-insulator transition based on Mott's minimum metallic conductivity (σ_{min}) criterion for a degenerately doped semiconductor[28]:

$$\sigma_{min} = (0.03)\left(\frac{e^2}{\hbar\, a_B}\right) \quad (1)$$

where a_B is the Bohr radius with its value between 2.5×10^{-7} cm and 5.0×10^{-7} cm for BSO assuming an effective mass (m^*) of 0.2 m_e–0.4 m_e (refs 22,29), and a dielectric constant of 20 (ref. 30). A small upturn in $\rho(T)$ was observed at low-temperatures and attributed to weakly localized transport. $\rho(T)$ increases with decreasing n_{3D} leading to a metal-to-insulator transition between $5.48\times10^{18}\,cm^{-3} < n_{3D} < 1.51\times10^{19}\,cm^{-3}$. The theoretical critical carrier density (n_C) for the Mott metal-to-insulator transition in an uncompensated, degenerately doped semiconductor is shown in ref. 28:

$$n_C = \left(\frac{0.26}{a_B}\right)^3 \quad (2)$$

Using equation 2, we calculate n_C for metal-to-insulator transition between $1\times10^{17}\,cm^{-3}$ to $1.0\times10^{18}\,cm^{-3}$, which is an order of magnitude smaller than our experimental value. This result suggests the existence of charge compensation in agreement with the presence of dislocations, as also observed in doped compensated semiconductors[31,32].

Next, we discuss the influence of charge compensation on n_{3D} and $\mu_{300\,K}$. Figure 2b shows a semi-log plot of room temperature n_{3D} as a function of inverse of T_{La}. It is noted that $1/T_{La}$ is directly related to the dopant density (N_{dopant}) as $N_{dopant} \propto e^{-\Delta/k_B T_{La}}$, where Δ and k_B are activation energy of evaporation of La, and the Boltzmann constant respectively. For low $1/T_{La}$ (high N_{dopant}), n_{3D} first decreases linearly on a logarithmic scale, as one would expect with increasing $1/T_{La}$ if La is the source of electron and if it is fully-activated (See Supplementary Fig. 5). For high $1/T_{La}$ (low N_{dopant}), n_{3D} however decreases faster, that is, deviates from linearity, indicating electrons are being trapped at the charged dislocations present in the film resulting in lower carrier concentration. This trend is in agreement with the charge compensation being operative below $n_{3D} \le 6.64\times10^{19}\,cm^{-3}$ (marked by an arrow) and is remarkably similar to the behaviour observed in doped III–N systems with dislocations[17–20,33]. Fig. 2c shows $\mu_{300\,K}$ versus n_{3D} for two series of samples: doped $Ba_{1-x}La_xSnO_3$ with a fixed cation stoichiometry but different x (red circle); and doped $Ba_{1-x-y}La_xSnO_3$ with a fixed x but different $y \ge 0$ (blue circle). It is noted that $y=0$ corresponds to the cation stoichiometric composition with $n_{3D}=2.53\times10^{20}$ and $\mu_{300\,K}=105\,cm^2\,V^{-1}\,s^{-1}$. The value of y, and thereby Ba vacancies V''_{Ba} was controlled by varying the Ba/Sn BEP at a fixed Ba BEP. We first discuss the stoichiometric samples (red circle) with different n_{3D}. We observe with decreasing carrier density, $4\times10^{20}\,cm^{-3} < n_{3D} < 1\times10^{21}\,cm^{-3}$, mobility first increases; then remain unchanged between 6.64×10^{19} and $4.06\times10^{20}\,cm^{-3}$ followed by a steeper decrease at $n_{3D} \le 6.64\times10^{19}\,cm^{-3}$ (marked by an arrow). Remarkably, the carrier density at which $\mu_{300\,K}$ begins to decrease is identical to the density at which non-linearity occurs and the compensation kicks-in, as illustrated in Fig. 2b. This result suggests the decrease in mobility for low n_{3D} is due to scattering and compensation from charged defects largely owing to dislocations in the film, and is remarkably similar to the prior results obtained from GaN thin films[19].

To further reveal scattering due to charged defects in low doping regime, we now turn to the second series of samples, $Ba_{1-x-y}La_xSnO_3$ where x was kept constant, and y (thereby V''_{Ba}) was varied (blue circle in Fig. 2c). We observe a reduction of n_{3D} accompanied by a decrease in mobility with increasing V''_{Ba}, in agreement with the theoretical prediction of Ba-vacancies being an acceptor-like defect[34]. Most importantly, we observe that the functional dependence of $\mu_{300\,K}$ versus n_{3D} is similar for both sets of samples in the low doping regime. Besides indicating a similar scattering potential around dislocation cores and Ba-vacancies, this result also suggests that the dislocation cores in nominally stoichiometric films may consist of Ba-vacancies. Future experimental and theoretical studies should clearly focus on studying the composition of dislocation cores and electrostatic scattering potentials around them.

Mobility-limiting scattering mechanisms. To get more insight into the transport in BSO films, we measured the temperature dependence of n_{3D} and μ for different dopant concentrations, as shown in Fig. 3. No carrier freeze-out was found down to 1.8 K for all measured electron concentrations (Fig. 3a), indicating that La-doped BSO forms a degenerate semiconductor. No T-dependence of the sample with electron concentration of $5.48\times10^{18}\,cm^{-3}$ is shown due to the non-ohmic contacts at $T<300$ K. A strong T-dependence of μ was observed for all films (Fig. 3b) indicating different scattering mechanisms at play.

To examine the role of individual carrier scattering mechanisms, we calculated μ as a function of T. For this purpose, we used AMSET: *ab initio* model for calculating the mobility and Seebeck

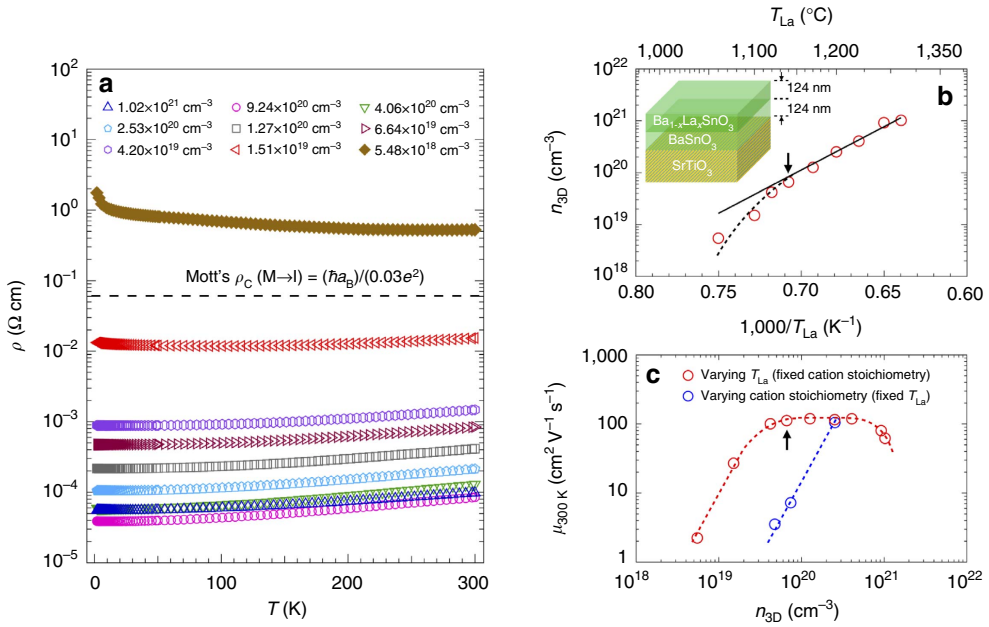

Figure 2 | Temperature dependence of resistivity and the influence of charge compensation on room temperature carrier density and mobility. (**a**) Resistivity (ρ) of doped $BaSnO_3$ films as a function of temperature (T) for different free carrier concentration measured at 300 K. (**b**) Free carrier concentration (n_{3D}) at 300 K as a function of La cell temperature (T_{La}) representing dopant concentration. Inset shows the schematic of the structure used, and (**c**) $\mu_{300\,K}$ versus n_{3D} for stoichiometric (red open circles) and Ba-deficient films (blue open circles). Non-stoichiometric films had 31 nm of buffer and active layer thicknesses. Black arrows mark the onset of charge compensation.

coefficient using the Boltzmann transport equation (BTE)[35,36]. AMSET has proven reliable for the calculation of mobility and Seebeck coefficient of several other semiconductors, including ZnS (ref. 37), GaAs and InN (ref. 35), whose transport properties are also governed by a single conduction band, like BSO. The model setup and parameters used are summarized in the method section, with additional details found in the literature[35]. In this model, the DFT band structure is used to calculate the group velocities of the carriers, which in turn are used to compute various carrier-scattering rates that enable us to explicitly solve the BTE; we then calculate the perturbation to the electronic distribution in the presence of low-electric field or thermal gradient, which gives us the mobility or Seebeck coefficient, respectively, of BSO. We considered both inelastic scattering (longitudinal polar optical phonon, (LO)) and elastic scattering (ionized impurity (IMP), acoustic phonon deformation potential (AC), transverse optical phonon (TO), piezoelectric (PE) and charged dislocation (DIS)) mechanisms. In our model, charged threading dislocations are treated as acceptor-like (negative charge) defects. We note that it is a reasonable assumption owing to its influence on the carrier density[38]. Moreover, it is also natural to think that in the presence of charged dislocations (negative charge), ionized dopants (positive charge) and electronic carrier (negative charge) in the doped BSO film, there must also exist other types of donor-like (positive charge) defects to maintain charge neutrality. We therefore can write a charge neutrality condition[35]:

$$n + Z_A N_A + \frac{Z_{DIS} N_{DIS}}{c_l} = Z_D N_D \qquad (3)$$

where Z represents the charge; A stands for acceptor ($-$ charge) and D for donor ($+$ charge); c_l is the lattice constant of $BaSnO_3$. Note the donor (N_D) here represents both charged dopants and other donor-like defects to compensate for charged dislocations. For n-doped BSO films, $N_D \gg N_A$ and thus acceptor term $Z_A N_A$ can be neglected. Using the formulation from refs 35,39, we define an overall ionized impurity concentration, N_{IMP} in our films as (assuming $N_A = 0$ as discussed above):

$$N_{IMP} = Z_A^2 N_A + Z_D^2 N_D = Z_D \left[\frac{Z_{DIS} N_{DIS}}{c_l} + n \right] \qquad (4)$$

where n is the electron concentration of the samples and Z_D is the charge state of the donor. Equation 4 shows how N_{IMP} depends not only on the electron concentration, n, but also on the concentration of charged threading dislocations, N_{DIS}. As seen in equation 5 (in method section), IMP scattering rate is proportional to N_{IMP}.

Figure 4 shows experimental (symbols) and calculated values (solid line) of μ versus T for three representative samples with n_{3D} belonging to low, intermediate and high density regimes of Fig. 2c. We also show individual contributions to the overall mobility due to different scattering mechanisms (dashed lines). We only show calculated mobility down to 20 K because below this temperature, the Fermi–Dirac distribution becomes step-like and the numerical integration of the distribution and density of state to calculate n_{3D} becomes unreliable. As N_{DIS}, Z_D and Z_{DIS} are not known for these samples, we use them as a fitting parameter for calculating μ, which yields $Z_D Z_{DIS} N_{DIS}$ between 7×10^{11} and $3 \times 10^{12}\,cm^{-2}$. Ionized impurities and dislocations both are charged defects; the overall functional dependence of μ on T thus remains same for the two scattering mechanisms. LO phonon scattering has a weak dependence on n_{3D}, and therefore remains nearly same for all three films. AC scattering, TO phonon scattering, and PE scattering, on the other hand, are dependent on n_{3D}. However, their dependence on n_{3D} becomes weaker at higher carrier concentrations.

Looking at the dominant scattering processes for films with low doping ($n_{3D} = 1.51 \times 10^{19}\,cm^{-3}$) and high doping ($n_{3D} = 1.02 \times 10^{21}\,cm^{-3}$), dislocation scattering and ionized impurity scattering limit the mobility respectively at all temperatures (Fig. 4a,c). However, for films with intermediate doping ($n_{3D} = 4.06 \times 10^{20}\,cm^{-3}$), mobility is mostly limited by ionized impurity scattering below 200 K (Fig. 4b), while at higher

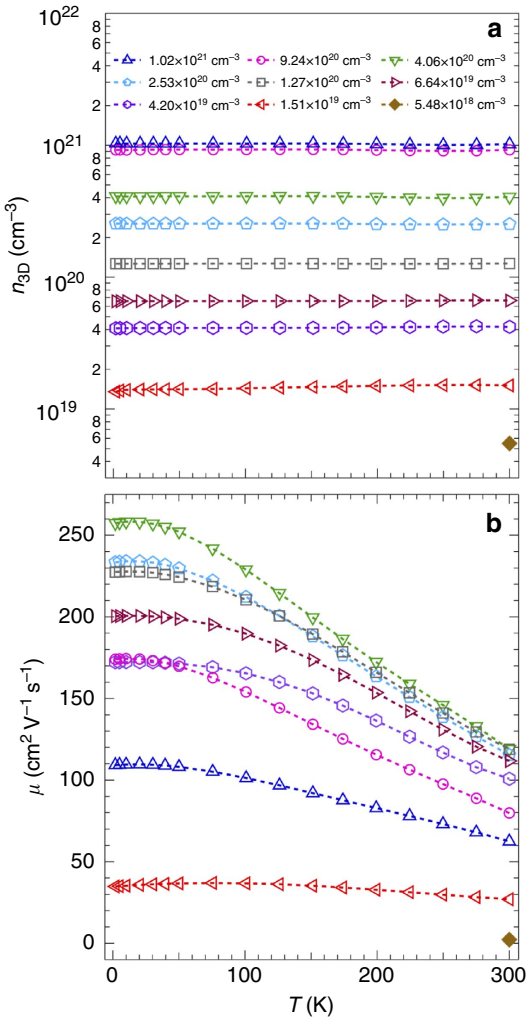

Figure 3 | Temperature dependence of carrier concentration and mobility. (**a**) n_{3D}, and (**b**) μ as a function of temperature (T) for doped BSO films with different n_{3D}.

temperatures mobility is governed by LO phonon scattering. Moreover, from Fig. 4a–c, dependence of μ_{IMP} on the concentration decreases for $n_{3D} = 1.02 \times 10^{21}\,cm^{-3}$, whereas it remained nearly unchanged between $n_{3D} = 1.51 \times 10^{19}\,cm^{-3}$ and $n_{3D} = 4.06 \times 10^{20}\,cm^{-3}$. This seems counter intuitive as one would naively think IMP scattering should increase with increasing n and therefore μ_{IMP} should decrease proportionately. We interpret this behaviour owing to a combined effect of N_{IMP} and the charge screening on IMP scattering with different doping density. For instance, using equation 4, the values of N_{IMP} are $7 \times 10^{19}\,cm^{-3}$ and $4.33 \times 10^{20}\,cm^{-3}$ for samples presented in Fig. 4a,b respectively (assuming $Z_D = 1$) suggesting higher μ_{IMP} in Fig. 4a if N_{IMP} is the only mobility-limiting factor. However on the other hand, the calculated inverse charge screening lengths, β for samples presented in Fig. 4a–c are about $0.57\,nm^{-1}$, $0.98\,nm^{-1}$, $0.98\,nm^{-1}$ respectively at 300 K implying increased IMP scattering rates (See method section) and lower μ_{IMP} for the sample in Fig. 4a. Using the same argument, lower μ_{IMP} in Fig. 4c can also be understood owing to increased N_{IMP}. See the method section for more information on charge screening.

Figure 4a–c further revealed n-dependence of μ_{DIS} increases from $n_{3D} = 1.51 \times 10^{19}\,cm^{-3}$ to $4.06 \times 10^{20}\,cm^{-3}$ and then decreases for $n_{3D} = 1.02 \times 10^{21}\,cm^{-3}$. Using β, we calculate the DIS scattering rate, which is larger for sample with $n_{3D} = 1.51 \times 10^{19}\,cm^{-3}$; and almost similar for other two samples. In addition, we found $Z_D Z_{DIS} N_{DIS}$ of 2.3×10^{12}, 7.0×10^{11} and $2.8 \times 10^{12}\,cm^{-2}$ for samples in Fig. 4a–c, respectively. Combining the effect of N_{DIS} and the charge screening on DIS scattering, μ_{DIS} is thus expected to possess the lowest value for sample with $n_{3D} = 1.51 \times 10^{19}\,cm^{-3}$, increasing for $n_{3D} = 1.02 \times 10^{21}\,cm^{-3}$ and being largest for $n_{3D} = 4.06 \times 10^{20}\,cm^{-3}$, as illustrated in Fig. 4.

As a further check of our model, we perform measurements and calculations of the Seebeck coefficients (S) as a function of n_{3D} (Fig. 5a). Inset shows T-dependent Seebeck coefficient for a representative sample with $n_{3D} = 4.06 \times 10^{20}\,cm^{-3}$, indicating negative S consistent with n-type carriers. Calculations of S were performed accounting for all the scattering mechanisms as described above for calculating μ, with and without N_{DIS}. Significantly, overall trend of experimental value of S versus n_{3D} is similar to the calculated values with dislocations, in agreement with our transport results. The calculation further reveals that the Seebeck coefficient is independent of N_{DIS} in the high doping regime whereas increasing N_{DIS} seems to enhance and then saturate the Seebeck coefficient in the low doping regime.

To further examine the self-consistency of AMSET model, we plot in Fig. 5b the calculated dependence of $\mu_{300\,K}$ versus n_{3D} for different N_{DIS}. $\mu_{300\,K}$ is also calculated for the case, when no dislocations are present. We overlay experimental values of $\mu_{300\,K}$ (red circles) on the same plot for comparison. The calculated values are again in good agreement with the experiment. The result suggests that our films may have different N_{DIS} despite of identical t_{buffer}, which may be due to different doping levels. We note that the calculated mobilities using AMSET are sometimes underestimated as the record room temperature mobility in bulk BSO has been $320\,cm^2\,V^{-1}\,s^{-1}$ at $n_{3D} = 8 \times 10^{19}\,cm^{-3}$, whereas the calculated value in Fig. 5b is $195\,cm^2\,V^{-1}\,s^{-1}$ at a similar doping level, so these values should be treated as lower bounds. Most importantly, in addition to providing numerous insights into electronic transport behaviour of $BaSnO_3$, our calculations also suggest directions for future experiments. For instance, calculations reveal the overall trend of $\mu_{300\,K}$ versus n_{3D} if there were no dislocations in the film. It tells that with decreasing n_{3D}, $\mu_{300\,K}$ with no dislocation will increase owing to reduced impurity scattering. For $5 \times 10^{18}\,cm^{-3} < n_{3D} < 4 \times 10^{19}\,cm^{-3}$, $\mu_{300\,K}$ is expected to decrease due to stronger interaction between low density electrons (that is, lower Fermi level) and optical phonons until electron-phonon interactions become much weaker (that is, reduced LO phonon scattering) resulting again in an increase of $\mu_{300\,K}$ for $n_{3D} < 5 \times 10^{18}\,cm^{-3}$. In contrast, mobility at low temperature (20 K) is expected to show a monotonically increasing behaviour with decreasing n_{3D}, reaching towards a value of $2{,}000\,cm^2\,V^{-1}\,s^{-1}$.

New outlook and opportunities. To benchmark our films with respect to the best wide gap oxide conductors, we show in Fig. 6 the highest reported value of room temperature conductivity σ (300 K) for different oxides, which are often used as metallic electrodes and TCOs in electronic applications. We also show the highest value of σ (300 K) of bulk BSO single crystals and thin films grown using different routes. Remarkably, the film grown using hybrid MBE possesses higher conductivity than those reported to-date both in the bulk BSO crystal and films, and is comparable to that of ITO, an industry standard for TCOs. We note that although high conductivity is achieved owing to high doping density and mobility, the ability of BSO to afford high conductivity without any phase segregation is very promising for fundamental study and application. For example, conductive BSO could be an ideal electrode material in oxide electronics providing

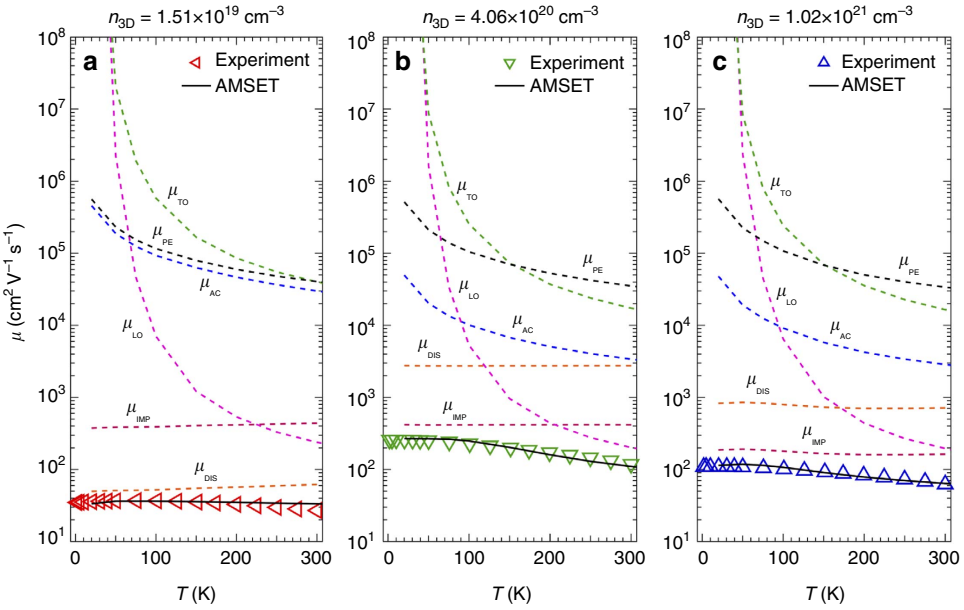

Figure 4 | Temperature dependence of mobility and individual contributions to the mobility from different scattering mechanisms. μ versus T for doped $BaSnO_3$ films, (**a**) $n_{3D} = 1.51 \times 10^{19}\,cm^{-3}$, (**b**) $n_{3D} = 4.06 \times 10^{20}\,cm^{-3}$, and (**c**) $n_{3D} = 1.02 \times 10^{21}\,cm^{-3}$. Contributions from different carrier scattering mechanisms are shown with dotted curves. Dislocation density as calculated from the model were—(**a**) $Z_D Z_{DIS} N_{DIS} = 2.3 \times 10^{12}\,cm^{-2}$, (**b**) $Z_D Z_{DIS} N_{DIS} = 7.0 \times 10^{11}\,cm^{-2}$, and (**c**) $Z_D Z_{DIS} N_{DIS} = 2.8 \times 10^{12}\,cm^{-2}$ respectively for the three samples, where Z_D and Z_{DIS} are the overall charge states of the donors and charged dislocations respectively. See method section for more details.

not only electrode function but also transparency, which could be vital for applications such as solar cells or display technologies. In addition, high conductivity of BSO could also be important for fundamental study and applications at high frequencies. High-frequency measurements and devices require low resistance contacts, where epitaxially-grown highly conductive BSO can play a significant role. Moreover, high conductivity of BSO films can also be beneficial for the investigation of ultra-fast phase dynamics of multiferroics without potential issues of charging effect. The major advantage of using conductive BSO as opposed to metals is its structural compatibility with these materials. Finally, the ability of BSO to accommodate high density of electrons and mobility along with wide bandgap makes it a suitable material candidate for ultra-high density quantum wells for plasmonic and power electronics applications.

Discussion. In summary, we have demonstrated the hybrid MBE approach for reproducible and controlled doping of epitaxial BSO on STO(001) with La. We establish a correlation between dislocation, V''_{Ba}, carrier density, mobility and metal-insulator transition in BSO. The combination of controlled doping, detailed electronic characterization, with modelling using the Boltzmann transport equations and an *ab initio* band structure calculations allow us to understand, tune and predict the transport behaviour and mobility limiting mechanisms in BSO. An important outcome of the study is that room temperature mobility in BSO films is limited by both defects, and electron-phonon scattering. The results place doped-BSO on par with highly successful III-Nitrides in terms of mobilities but with the added benefit of having high carrier concentrations for high-power oxide electronics operating at room temperature.

Methods

Growth and characterization of $BaSnO_3$ films. Details of our hybrid MBE approach for stoichiometric BSO heteroepitaxy are discussed elsewhere[21,25]; a brief description will be provided here. BSO films were grown via hybrid molecular beam epitaxy (hybrid MBE). Hexamethylditin was used as the metal-organic chemical precursor for Sn. Ba and La were evaporated using effusion cells, and oxygen was supplied using an RF plasma source. The oxygen pressure and substrate temperature were fixed at 5×10^{-6} torr and 900 °C respectively for all growths. A 350-nm-thick Ta layer was deposited on the back of the substrates to improve heat transfer between the film and the substrate heater. Substrates were cleaned in oxygen plasma for 20 min before film growth ensuring no carbon contamination was present at the surface. Dopant density in the films was controlled by varying La-cell temperature ($1060\,°C \leq T_{La} \leq 1290\,°C$). Films were annealed after growth in oxygen using rapid thermal annealer at 800 °C for 2 min to ensure oxygen stoichiometry. All substrates after film growth and undoped films were confirmed to be insulating ($\rho > 10^5\,\Omega\,cm$). Electronic transport measurements were performed in a Quantum Design Physical Property Measurement System (DynaCool) using indium as ohmic contacts in a van der Pauw geometry. Thermopower measurements were performed with a home built system described elsewhere[40].

AMSET and DFT calculation details. The AMSET model employs materials parameters that were obtained from the experimental literature, as listed in Table 1. In this work, the primary purpose of the AMSET model is to explain the observed experimental phenomena, so it is appropriate to use experimental parameters even though the same values can be calculated *ab initio* with only minor deviations to the resulting mobility and Seebeck coefficient. For instance, deformation potential (E_D) is calculated *ab initio*. We, however, emphasize that the choice of deformation potential in our calculations, even if an order of magnitude different than the value reported in Table 1 does not influence our interpretation of mobility data. It is noted that the mobility due to AC scattering, which uses E_D is not limiting at any temperature or concentration. The same holds true for the values of the elastic constants that were extracted from DFT generalized gradient approximation of Perdew, Burke and Ernzerhof (GGA-PBE) calculations[41]; these have essentially no effect on the overall mobility, as the mobility due to AC scattering is always orders of magnitude higher than the actual limiting mechanisms.

To calculate the electronic band structure of BSO, the unit cell was optimized using Kohn–Sham density functional theory (KS-DFT)[42,43] as implemented in the Vienna *ab initio* Simulation Package[44–47]. We used the generalized gradient approximation of Perdew, Burke and Ernzerhof[48] (GGA-PBE) to express the exchange-correlation potential and Projector Augmented Wave potentials to represent the wave functions. On geometry optimization, the lattice constant (0.419 nm) was increased by 1.76% compared to the experimental value (0.412 nm). This is a common behaviour when using a GGA-PBE functional, due to delocalization of electrons. We used a **k**-point mesh of $6 \times 6 \times 6$ for self-consistent calculations, as adding more **k**-points results in <0.01 eV difference in total energy. The energy cutoff for the plane wave basis set was set to 520 eV in all calculations.

For electronic properties calculations, we chose the **k**-points closest to the conduction band minimum (CBM), which for $BaSnO_3$ is at the Γ-point. An adaptive **k**-points mesh was used, which is denser close to the CBM. We used the AMSET code[35] to calculate the mobility and the Seebeck coefficient, which uses the

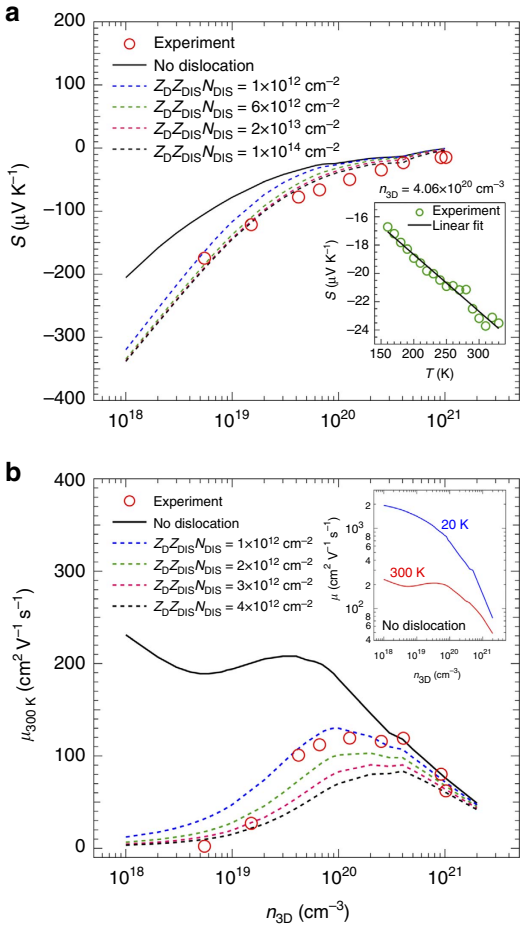

Figure 5 | Comparison of experimental and calculated values of Seebeck coefficient and mobility as a function of carrier concentration with and without dislocations. (**a**) Seebeck coefficients (S) of doped $BaSnO_3$ films at 300K as a function of n_{3D}. Experimental data are shown as red circles and calculated values are represented using solid line for no dislocation, and using dotted lines for different $Z_D Z_{DIS} N_{DIS}$. Inset shows the T-dependent S for $n_{3D} = 4.06 \times 10^{20}\,cm^{-3}$, consistent with n-type conduction. (**b**) Room-temperature mobility ($\mu_{300\,K}$) as a function of n_{3D}. Experimental data are shown in red circles while calculated values are represented with solid (without dislocation) and dotted lines (with varying dislocation density). Inset shows the variation of μ at two different temperatures (300 K and 20 K) for films with no dislocation.

DFT band structures to solve the BTE. The explicit solution to BTE is particularly important for the inelastic LO-phonon scattering mechanism as it is the major limiting mechanism for the sample with $n_{3D} = 4.06 \times 10^{20}\,cm^{-3}$, for $T > 200$ K (Fig. 4b). More information on the LO-scattering can be found elsewhere[35,39]. On the other hand, two other major elastic scattering mechanisms in BSO are ionized impurity (IMP) and charged dislocation scattering (DIS). We note that it is the threading dislocations in the active layer, which limit the mobility. Misfit dislocations on the other hand are pinned at the film/substrate interface making themselves electrically separated from the active layer where electronic transport is measured. We write the expressions used to model these scattering phenomena from refs 35,39 to clarify how these scattering rates and necessary parameters are calculated. The IMP and DIS scattering rates, v, are expressed via the following equations:

$$v_{IMP}(k) = \frac{e^4 N_{IMP}}{8\pi\varepsilon_0^2 \hbar^2 k^2 v(k)} \left[D(k) \ln\left(1 + \frac{4k^2}{\beta^2}\right) - B(K) \right] \quad (5)$$

$$v_{DIS}(k) = \frac{Z_{DIS}^2 N_{DIS} e^4 k}{\varepsilon_0^2 \hbar^2 c_l^2 v(k)} \left(1 + \frac{4k^2}{\beta^2}\right)^{-3/2} \beta^{-4} \quad (6)$$

$$\beta^2 = \frac{e^2}{\varepsilon_0 k_B T} \int D_s(E) f(E)[1 - f(E)] dE \quad (7)$$

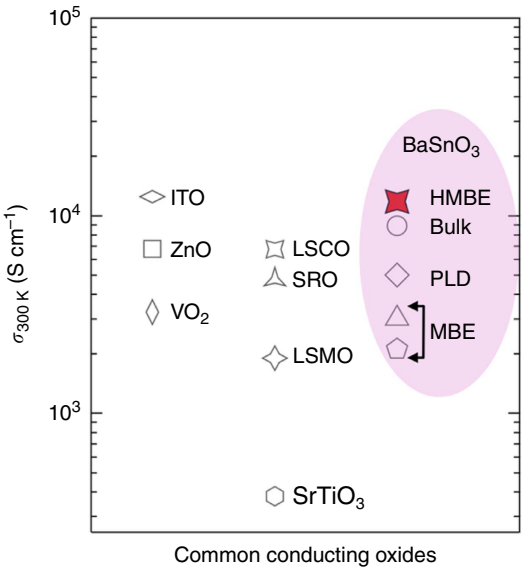

Figure 6 | Comparison of conductivity values for common conducting oxides. Compilation of highest room temperature conductivity $\sigma_{300\,K}$ of $BaSnO_3$ bulk single crystal and films grown by various deposition techniques (taken from refs 9,16,22) including hybrid molecular beam epitaxy. The highest known $\sigma_{300\,K}$ for common transparent conducting oxides (ITO = indium tin oxide, ZnO) and other metallic oxides as conductive electrodes for high frequency applications (VO_2, LSCO = $La_{0.5}Sr_{0.5}CoO_3$, $SrTiO_3$, LSMO = $La_{0.7}Sr_{0.3}MnO_3$, SRO = $SrRuO_3$) are shown for comparison (refs 49–55).

Table 1 | Input parameters to our AMSET model using *ab initio* calculations and using experimental values.

Model parameters	*Ab initio*	Experiments[56]
Polar optical phonon frequency, ω_{PO} (THz)	20.36	**12.23**
Low-frequency dielectric constant, ε_0	5.2	**17 ± 2**
High-frequency dielectric constant, ε_∞	3.4	**3.3**
Deformation potential, E_D (eV)	**6.19**	-

The bold numbers indicate parameters that are used in our calculations.

where k is the magnitude of the wave vector, E is the energy, β is the inverse screening length due to charge defects, ε_0 is the static dielectric constant, e is the charge of an electron, c_l is the lattice parameter of BSO, $v(k)$ is the group velocity of electron which is directly derived from the DFT band structure, Z_{DIS} is the charge state of dislocations, $B(K)$ and $D(K)$ are parameters describing the non-parabolicity of the conduction band, which are directly derived from the DFT band structure, D_s is the density of states and k_B is the Boltzmann constant. We further note that to calculate the mobility values, $Z_D Z_{DIS} N_{DIS}$ is used as a fitting parameter instead of N_{DIS} as the charge states of the donor (defined as charged dopants and other donor-like defects to compensate for charged dislocations) and dislocations are not known. It is interesting to note that the screening lengths are the same in Fig. 4b,c both of which have very high concentrations indicating a highly degenerate semiconductor or essentially a metal. In fact, the calculated Fermi level for Fig. 4a is 0.15 eV inside the conduction band (above the CBM) while that is 0.94 and 1.03 eV for samples with higher n_{3D}. At such high concentrations, the departure from uniformity of the free-electron concentration in presence of a potential surrounding an impurity, δn, becomes insensitive to the concentration itself. δn is directly related to charge screening. See ref. 38 for more details.

Data availability. The data that support the main findings of this study are available from the corresponding authors on request.

References

1. Heber, J. Enter the oxides. *Nature* **459,** 28–30 (2009).
2. Schlom, D. G. & Mannhart, J. Oxide electronics: interface takes charge over Si. *Nat. Mater.* **10,** 168–169 (2011).

3. Jin, S. *et al.* Thousandfold change in resistivity in magnetoresistive La-Ca-Mn-O Films. *Science* **264,** 413–415 (1994).
4. The interface is still the device. *Nat. Mater.* **11,** 91 (2012).
5. Hwang, H. Y. *et al.* Emergent phenomena at oxide interfaces. *Nat. Mater.* **11,** 103–113 (2012).
6. Schlom, D. G. & Pfeiffer, L. N. Oxide electronics: upward mobility rocks! *Nat. Mater.* **9,** 881–883 (2010).
7. Luo, X. *et al.* High carrier mobility in transparent $Ba_{1-x}La_xSnO_3$ crystals with a wide band gap. *Appl. Phys. Lett.* **100,** 172112 (2012).
8. Kim, H. J. *et al.* High mobility in a stable transparent perovskite oxide. *Appl. Phys. Exp.* **5,** 061102 (2012).
9. Kim, H. J. *et al.* Physical properties of transparent perovskite oxides (Ba,La)SnO_3 with high electrical mobility at room temperature. *Phys. Rev. B* **86,** 165205 (2012).
10. Beigi, S. I., Walker, F. J., Cheong, S. W., Rabe, K. M. & Ahn, C. H. Alkaline earth stannates: The next silicon? *APL Mater.* **3,** 062510 (2015).
11. Singh, D. J., Xu, Q. & Ong, K. P. Strain effects on the band gap and optical properties of perovskite $SrSnO_3$ and $BaSnO_3$. *Appl. Phys. Lett.* **104,** 011910 (2014).
12. Alaan, U. S., Shafer, P., Diaye, A. T., Arenholz, E. & Suzuki, Y. Gd-doped $BaSnO_3$: a transparent conducting oxide with localized magnetic moments. *Appl. Phys. Lett.* **108,** 042106 (2016).
13. Chambers, S. A., Kaspar, T. C., Prakash, A., Haugstad, G. & Jalan, B. Band alignment at epitaxial $BaSnO_3/SrTiO_3(001)$ and $BaSnO_3/LaAlO_3(001)$ heterojunctions. *Appl. Phys. Lett.* **108,** 152104 (2016).
14. Krishnaswamy, K. *et al.* $BaSnO_3$ as a channel material in perovskite oxide heterostructures. *Appl. Phys. Lett.* **108,** 083501 (2016).
15. Tsukazaki, A. *et al.* Quantum hall effect in polar oxide heterostructures. *Science* **315,** 1388–1391 (2007).
16. Raghavan, S. *et al.* High-mobility $BaSnO_3$ grown by oxide molecular beam epitaxy. *APL Mater.* **4,** 016106 (2016).
17. Elsner, J. *et al.* Deep acceptors trapped at threading-edge dislocations in GaN. *Phys. Rev. B* **58,** 12571–12574 (1998).
18. Gurusinghe, M. N. & Andersson, T. G. Mobility in epitaxial GaN: limitations of free-electron concentration due to dislocations and compensation. *Phys. Rev. B* **67,** 235208 (2003).
19. You, J. H., Lu, J.-Q. & Johnson, H. T. Electron scattering due to threading edge dislocations in n-type wurtzite GaN. *J. Appl. Phys.* **99,** 033706 (2006).
20. Ng, H. M., Doppalapudi, D., Moustakas, T. D., Weimann, N. G. & Eastman, L. F. The role of dislocation scattering in n-type GaN films. *Appl. Phys. Lett.* **73,** 821–823 (1998).
21. Prakash, A. *et al.* Adsorption-controlled growth and influence of stoichiometry on electronic transport in hybrid molecular beam epitaxy-grown $BaSnO_3$ films. *J. Mater. Chem. C* doi:10.1039/c7tc00190h (2017).
22. Higgins, Z. L. *et al.* Direct observation of electrostatically driven band gap renormalization in a degenerate perovskite transparent conducting oxide. *Phys. Rev. Lett.* **116,** 027602 (2016).
23. Ganguly, K. *et al.* Structure and transport in high pressure oxygen sputter-deposited $BaSnO_{3-\delta}$. *APL Mater.* **3,** 062509 (2015).
24. Lee, W.-J. *et al.* Enhanced electron mobility in epitaxial (Ba,La)SnO_3 films on $BaSnO_3(001)$ substrates. *Appl. Phys. Lett.* **108,** 082105 (2016).
25. Prakash, A. *et al.* Hybrid molecular beam epitaxy for the growth of stoichiometric $BaSnO_3$. *J. Vac. Sci. Technol. A* **33,** 060608 (2015).
26. Nakamura, S. GaN Growth Using GaN Buffer Layer. *Jap. J. Appl. Phys.* **30,** L1705–L1707 (1991).
27. Park, C. *et al.* High mobility field effect transistor based on $BaSnO_3$ with Al_2O_3 gate oxide. *Appl. Phys. Lett.* **105,** 203503 (2014).
28. Mott, N. F. The minimum metallic conductivity. *Int. Rev. in Phys. Chem.* **4,** 1–18 (1985).
29. Allen, S. J., Raghavan, S., Schumann, T., Law, K.-M. & Stemmer, S. Conduction band edge effective mass of La-doped $BaSnO_3$. *Appl. Phys. Lett.* **108,** 252107 (2016).
30. Singh, P. *et al.* Electronic structure, electrical and dielectric properties of $BaSnO_3$ below 300 K. *Jap. J. Appl. Phys.* **47,** 3540–3545 (2008).
31. Poklonski, N. A., Vyrko, S. A. & Zabrodskii, A. G. Electrostatic models of insulator-metal and metal-insulator concentration phase transitions in Ge and Si crystals doped by hydrogen-like impurities. *Phys. Sol. State* **46,** 1101–1106 (2004).
32. Shklovskii, B. I. & Efros, A. L. *Electronic Properties of Doped Semiconductors* (Springer, 1984).
33. Miller, N. *et al.* Effect of charged dislocation scattering on electrical and electrothermal transport in n-type InN. *Phys. Rev. B* **84,** 075315 (2011).
34. Scanlon, D. O. Defect engineering of $BaSnO_3$ for high-performance transparent conducting oxide applications. *Phys. Rev. B* **87,** 161201 (2013).
35. Faghaninia, A., Ager, J. W. & Lo, C. S. *Ab initio* electronic transport model with explicit solution to the linearized Boltzmann transport equation. *Phys. Rev. B* **91,** 235123 (2015).
36. Faghaninia, A., Ager, III J. W. & Lo, C. S. *Ab initio* Model for Mobility and Seebeck coefficient using Boltzmann Transport (aMoBT) equation https://nanohub.org/resources/22339 (2016).
37. Faghaninia, A., Bhatt, K. R. & Lo, C. Alloying ZnS in the wurtzite phase to create high-performing transparent conducting materials. *Phys. Chem. Chem. Phys.* **18,** 22628–22635 (2016).
38. Mun, H. *et al.* Large effects of dislocations on high mobility of epitaxial perovskite $Ba_{0.96}La_{0.04}SnO_3$ films. *Appl. Phys. Lett.* **102,** 252105 (2013).
39. Rode, D. L. *Low-field Electron Transport* Vol. 10 (Academic Press, 1975).
40. Ager, J. W. *et al.* Mg-doped InN and InGaN – photoluminescence, capacitance–voltage and thermopower measurements. *Physica Status Solidi* **245,** 873–877 (2008).
41. Bouhemadou, A. & Haddadi, K. Structural, elastic, electronic and thermal properties of the cubic perovskite-type $BaSnO_3$. *Solid State Sci.* **12,** 630–636 (2010).
42. Hohenberg, P. & Kohn, W. Inhomogeneous electron gas. *Phys. Rev.* **136,** B864–B871 (1964).
43. Kohn, W. & Sham, L. J. Self-consistent equations including exchange and correlation effects. *Phys. Rev.* **140,** A1133–A1138 (1965).
44. Kresse, G. & Hafner, J. *Ab initio* molecular dynamics for liquid metals. *Phys. Rev. B* **47,** 558–561 (1993).
45. Kresse, G. & Hafner, J. *Ab initio* molecular-dynamics simulation of the liquid-metal-amorphous-semiconductor transition in germanium. *Phys. Rev. B* **49,** 14251–14269 (1994).
46. Kresse, G. & Furthmuller, J. Efficiency of ab-initio total energy calculations for metals and semiconductors using a plane-wave basis Set. *Comput. Mater. Sci.* **6,** 15–50 (1996).
47. Kresse, G. & Furthmuller, J. Efficient iterative schemes for *ab initio* total-energy calculations using a plane-wave basis set. *Phys. Rev. B* **54,** 11169–11186 (1996).
48. Perdew, J. P., Burke, K. & Ernzerhof, M. Generalized gradient approximation made simple. *Phys. Rev. Lett.* **77,** 3865–3868 (1996).
49. Tashman, J. W. *et al.* Epitaxial growth of VO_2 by periodic annealing. *Appl. Phys. Lett* **104,** 063104 (2014).
50. Igasaki, Y. & Hiromi, S. The effects of deposition rate on the structural and electrical properties of ZnO: Al films deposited on (1120) oriented sapphire substrates. *J. Appl. Phys.* **7,** 3613–3619 (1991).
51. Ohta, H. *et al.* Highly electrically conductive indium–tin–oxide thin films epitaxially grown on yttria-stabilized zirconia (100) by pulsed-laser deposition. *Appl. Phys. Lett.* **76,** 2740–2742 (2000).
52. Cheung, J. T., Morgan, P. E. D., Lowndes, D. H., Zheng, X. Y. & Breen, J. Structural and electrical properties of $La_{0.5}Sr_{0.5}CoO_3$ epitaxial films. *Appl. Phys. Lett.* **62,** 2045–2047 (1993).
53. Koster, G. *et al.* Structure, physical properties, and applications of $SrRuO_3$ thin films. *Rev. Mod. Phys.* **84,** 253–298 (2012).
54. Adamo, C. *et al.* Effect of biaxial strain on the electrical and magnetic properties of (001) $La_{0.7}Sr_{0.3}MnO_3$ thin films. *Appl. Phys. Lett.* **95,** 112504 (2009).
55. Janotti, A., Jalan, B., Stemmer, S. & Walle, C. G. V. d. Effects of doping on the lattice parameter of $SrTiO_3$. *Appl. Phys. Lett.* **100,** 262104 (2012).
56. Stanislavchuk, T. N., Sirenko, A. A., Litvinchuk, A. P., Luo, X. & Cheong, S. W. Electronic band structure and optical phonons of $BaSnO_3$ and $Ba_{0.97}La_{0.03}SnO_3$ single crystals: Theory and experiment. *J. Appl. Phys.* **112,** 044108 (2012).

Acknowledgements

We thank Dr Greg Haugstad for help with the RBS measurements. This work was primarily supported by National Science Foundation through DMR-1410888, and in part by (specifically, electronic transport and modelling) the Young Investigator Program of the Air Force Office of Scientific Research (AFOSR) through Grant FA9550-16-1-0205. We also acknowledge the use of PPMS system, which has received capital equipment funding from the NSF through the UMN MRSEC program under Award Number DMR-1420013. Parts of this work were carried out at the Minnesota Nano Center and Characterization Facility, University of Minnesota, which receives partial support from NSF through the MRSEC program. Seebeck coefficient measurements were performed within the Electronic Materials Program, which is supported by Director, Office of Science, Office of Basic Energy Sciences, Materials Sciences and Engineering Division, of the U.S. Department of Energy under Contract No. DE-AC02-05CH11231. Band structure calculations and AMSET modelling were supported by the US-India Partnership for Advanced Clean Energy-Research (PACE-R) for the Solar Energy Research Institute for India and the United States (SERIIUS), funded jointly by the U.S. Department of Energy (Office of Science, Office of Basic Energy Sciences, and Energy Efficiency and Renewable Energy, Solar Energy Technology Program, under Subcontract DE-AC36-08GO28308 to the National Renewable Energy Laboratory, Golden, Colorado) and the Government of India, through the Department of Science and Technology under Subcontract IUSSTF/JCERDC-SERIIUS/2012 dated 22nd Nov. 2012. S.S. acknowledges support from the Singapore Berkeley Research Initiative for Sustainable Energy (SinBeRISE), funded by the National Research Foundation of Singapore. P.X. would like to acknowledge the support from the UMN Doctoral Dissertation Fellowship.

Author contributions

B.J. and A.P. conceived and designed the experiments; A.P. grew the samples, measured and analysed the transport data; P.X. carried out the transport measurement; C.S.L. and A.F. performed transport modelling; S.S. and J.W.A. III performed Seebeck measurements; and all authors discussed the results.

Additional information

Supplementary Information accompanies this paper at http://www.nature.com/naturecommunications

Competing interests: The authors declare no competing financial interests.

Reprints and permission information is available online at http://npg.nature.com/reprintsandpermissions/

How to cite this article: Prakash, A. *et al.* Wide bandgap $BaSnO_3$ films with room temperature conductivity exceeding 10^4 S cm^{-1}. *Nat. Commun.* **8,** 15167 doi: 10.1038/ncomms15167 (2017).

Publisher's note: Springer Nature remains neutral with regard to jurisdictional claims in published maps and institutional affiliations.